

This is the author's final, peer-reviewed manuscript as accepted for publication (AAM). The version presented here may differ from the published version, or version of record, available through the publisher's website. This version does not track changes, errata, or withdrawals on the publisher's site.

Electron acceleration by wave turbulence in a magnetized plasma

A. Rigby, F. Cruz, B. Albertazzi, R. Bamford, A. R. Bell, J. E. Cross, F. Fraschetti, P. Graham, Y. Hara, P. M. Kozlowski, Y. Kuramitsu, D. Q. Lamb, S. Lebedev, J. R. Marques, F. Miniati, T. Morita, M. Oliver, B. Reville, Y. Sakawa, S. Sarkar, C. Spindloe, R. Trines, P. Tzeferacos, L. O. Silva, R. Bingham, M. Koenig, and G. Gregori

Published version information

Citation: A Rigby et al. "Electron acceleration by wave turbulence in a magnetized plasma." *Nature Physics*, vol. 14 (2018): 475-479.

DOI: [10.1038/s41567-018-0059-2](https://doi.org/10.1038/s41567-018-0059-2)

This version is made available in accordance with publisher policies. Please cite only the published version using the reference above. This is the citation assigned by the publisher at the time of issuing the AAM. Please check the publisher's website for any updates.

This item was retrieved from **ePubs**, the Open Access archive of the Science and Technology Facilities Council, UK. Please contact epubs@stfc.ac.uk or go to <http://epubs.stfc.ac.uk/> for further information and policies.

Electron Acceleration by Wave Turbulence in a Magnetized Plasma

A. Rigby¹, F. Cruz², B. Albertazzi³, R. Bamford⁴, A. R. Bell¹, J. E. Cross¹, F. Fraschetti⁵, P. Graham⁶, Y. Hara⁷, P. M. Kozlowski¹, Y. Kuramitsu^{8,9}, D. Q. Lamb¹⁰, S. Lebedev¹¹, J. R. Marques³, F. Miniati¹², T. Morita⁷, M. Oliver¹, B. Reville¹³, Y. Sakawa⁷, S. Sarkar^{1,14}, C. Spindloe⁴, R. Trines⁴, P. Tzeferacos^{1,10}, L. O. Silva², R. Bingham^{4,15}, M. Koenig³, and G. Gregori^{1,10}

¹Department of Physics, University of Oxford, Parks Road, Oxford
OX1 3PU, UK

²GoLP/Instituto de Plasmas e Fusão Nuclear, Instituto Superior
Técnico, Universidade de Lisboa, 1049-001 Lisbon, Portugal

³Laboratoire pour l'Utilisation de Lasers Intenses, UMR7605,
CNRS CEA, Université Paris VI Ecole Polytechnique, 91128
Palaiseau Cedex, France

⁴Rutherford Appleton Laboratory, Chilton, Didcot OX11 0QX, UK

⁵Departments of Planetary Sciences and Astronomy, University of
Arizona, Tucson, AZ 85721, USA

⁶AWE, Aldermaston, Reading, West Berkshire RG7 4PR, UK

⁷Institute of Laser Engineering, Osaka University, 2-6 Yamadaoka,

Suita, Osaka 565-0871, Japan

⁸Department of Physics, National Central University, Taoyuan
320, Taiwan

⁹Graduate School of Engineering, Osaka University, 2-1
Yamadaoka, Suita, Osaka 565-0871, Japan

¹⁰Department of Astronomy and Astrophysics, University of
Chicago, 5640 S. Ellis Ave, Chicago, IL 60637, USA

¹¹Imperial College London, London, SW72AZ, UK

¹²Physics Department, Wolfgang-Pauli-Strasse 27, ETH-Zürich,
CH-8093 Zürich, Switzerland

¹³School of Mathematics and Physics, Queens University Belfast,
Belfast BT7 1NN, UK

¹⁴Niels Bohr Institute, Blegdamsvej 17, 2100, Copenhagen Ø,
Denmark

¹⁵Department of Physics, University of Strathclyde, Glasgow G4
0NG, UK

Astrophysical shocks are commonly revealed by the non-thermal emission of energetic electrons accelerated in-situ [1, 2, 3]. Strong shocks are expected to accelerate particles to very high energies [4, 5, 6], however, they require a source of particles with velocities fast enough to permit multiple shock crossings. Whilst the resulting diffusive shock acceleration [4] process can account for observations, the kinetic physics regulating the continuous injection of non-thermal particles is not well understood. Indeed, this injection problem is particularly acute for

electrons, which rely on high frequency plasma fluctuations to raise them above the thermal pool [7, 8]. Here we show, using laboratory laser-produced shock experiments, that in the presence of a strong magnetic field, significant electron pre-heating is achieved. We demonstrate that the key mechanism in producing these energetic electrons is through the generation of lower-hybrid turbulence via shock-reflected ions. Our experimental results are analogous to many astrophysical systems, including the interaction of a comet with the Solar-wind [9], a setting where electron acceleration via lower-hybrid waves is possible.

Lower-hybrid waves occur in a variety of laboratory and space environments. They have been suggested to be an important electron-heating or energization mechanism in different magnetized plasma environments [10, 11, 12]. These waves propagate nearly transverse to the magnetic field lines and oscillate at a frequency between the ion gyro frequency and the electron gyro frequency. As a consequence lower-hybrid waves with frequency ω and wavenumber \mathbf{k} can be in simultaneous Cerenkov resonance, $\omega - \mathbf{k} \cdot \mathbf{v} = 0$ (where \mathbf{v} is the particle velocity) both with magnetized electrons propagating along the field lines and unmagnetized ions moving perpendicular to the field. The lower-hybrid waves have a high phase velocity along the field lines that resonate with the fast moving electrons as well as a low phase velocity across the field lines that resonate with the slow moving ions, allowing for energy transfer between the two species [13] (see Methods for further details). This convenient property of lower-hybrid waves, as an efficient channel for the acceleration of electrons above the thermal background, is well known in the magnetically confined fusion community [14] where it has been exploited with considerable efficacy in past experiments [15, 16]. Although a different mechanism is favoured in toroidal field configurations, for highly oblique shocks such as might be created in the Solar wind [9], supernova explosions [11], or during the formation of galaxy clusters [17], it

is thought that the modified two-stream instability [13] driven by reflected ions from the shock front, excites broad-band lower-hybrid modes. By comparing theoretical and numerical predictions with the experimental data on the modified two-stream instability, it may be possible to develop robust scaling relations to apply to the fusion relevant parameters (see Methods for further discussion).

While electron acceleration by lower-hybrid waves in the Solar system has been inferred from satellite measurements [18, 9], laboratory experiments provide reproducible and controllable conditions that can be used not only as a means of supporting space observations, but also for validating multi-scale transport predictions from simulation codes [19]. Here we show the results from an experiment where a laser-produced plasma flow impacts on a magnetized sphere (see Figure 1). This mimics, for example, the interaction of the Solar-wind plasma with a comet [9], an environment where excess X-ray generation by accelerated electrons has been observed. The scaling between the experiment and the comet interaction with the Solar wind is determined by a set of parameters shown in Table 1 of Methods. While both lower-hybrid turbulence and charge exchange processes [20] are possible explanations, our experimental results are compatible only with the former (see Supplementary Information).

The experiment was conducted at the LULI laser facility at École Polytechnique (France). Various diagnostics were implemented to probe the plasma before and after the interaction with the sphere (see Figure 2 for details).

Streaked optical pyrometry (SOP) shows the optical plasma emission streaked in time. SOP indicates that the plasma travels at a velocity of 70 km/s, implying the fluorine ions have a kinetic energy ~ 500 eV. The interferometry data shows that for the magnetized sphere, there is a bulk electron density of $\sim 10^{17}$ cm $^{-3}$ upstream of the shock, rising to 10^{18} cm $^{-3}$ downstream of the shock. Optical spectroscopy data gives a bulk plasma temperature of 3 ± 1 eV.

The optical data indicates that the interaction of the plasma with the sphere is different for the magnetized and non-magnetized cases (see e.g., [21]). For the non-magnetized sphere, there is less pronounced plasma build up in front of the sphere.

Near the axis of the flow and close to the surface of the sphere a shock with ~ 1 mm stand-off distance can be seen. In the magnetized case, the perpendicular field lines constrain the flow, making it more difficult for the plasma to fully flow around the sphere. Consequently, there is a larger pressure build up in front of the sphere, generating a shock at ~ 2.5 mm stand-off position, larger than that of the non-magnetized case. Balancing the ram pressure of the plasma flow with that of the compressed magnetic field gives an estimation for the expected stand-off distance in the magnetized case of ~ 1 mm, similar to the experimental value.

To further understand the flow dynamics and its interaction with the sphere, 2-dimensional radiation-magnetohydrodynamics (MHD) simulations were performed using the FLASH code (see Supplementary Information). The simulations agree qualitatively with experimental measurements, as shown in Figure 2, while providing additional estimates of bulk plasma properties. The magnetic field carried by the ablated plasma is weak, and from the measured plasma parameters we infer the shock formed to be highly super-critical with a fast magneto-sonic Mach number of 5.7 ± 0.2 , necessitating a significant reflected ion component [22]. The electric field influencing the plasma near the shock can be estimated using the magnetic field and ion density calculated in FLASH (see Supplementary Information).

For the shock to reflect incoming ions, the cross-shock electric potential must exceed the kinetic energy of the incoming ions. FLASH simulations predict an electric field of ~ 70 MeV/m at a distance of 0.5 mm from the sphere at 300

ns, increasing as the simulation progresses. Assuming a shock thickness on the order of the electron skin-depth $L \sim 10 \mu\text{m}$ results in a cross-shock potential $\approx 700 \text{ eV}$, sufficient to reflect incoming Fluorine ions, with kinetic energy of $\sim 500 \text{ eV}$. These reflected ions produce the counter-streaming ion flow, which are necessary for generating lower-hybrid turbulence, an effect not captured in FLASH simulations.

We have probed the plasma emission in the soft X-ray range (630-770 eV) with an X-ray spectrometer that spatially resolved along the flow axis (see Supplementary Information). The integrated intensity of the observed Fluorine X-ray line can then be plotted as a function of position along the flow axis (see Figure 3). When the magnetized sphere is present an excess in X-ray intensity is observed close to the sphere compared with the non-magnetized sphere. This excess in soft X-rays suggests that electrons of energies significantly greater than 3 eV must be present. As lower-hybrid turbulence requires the reflected ions to move perpendicularly to the field lines, we have also considered the case when the sphere was rotated to have the magnetic dipole moment aligned with the flow, mimicking a parallel field line configuration. In the latter configuration, we found no appreciable increase in X-ray intensity close to the sphere relative to the non-magnetized case.

To investigate further the lower-hybrid origin for the excess X-ray emission near the magnetized sphere and the possible presence of a suprathermal electron population, we have performed 2D particle-in-cell (PIC) simulations of the plasma flow collision with the dipolar magnetic object (see Figure 4) using the massively parallel, fully relativistic code OSIRIS (see Supplementary Information).

OSIRIS simulation results indicate, in agreement with our previous FLASH simulations, that as the plasma impacts the sphere (of typical size larger than

the ion Larmor radius), a bow shock develops [23]. The counter-propagating ion flow is unstable and excites plasma waves in the lower-hybrid range ahead of the shock front (see Figure 4). These waves are then amplified and break, resulting in a turbulent, compressed plasma region. In fact the ratio between the parallel (k_{\parallel}) and perpendicular (k_{\perp}) wavenumber of these modes is consistent with the idealised dispersion relation for lower-hybrid waves of $\frac{k_{\parallel}}{k_{\perp}} \approx \sqrt{\frac{m_e}{m_i}}$ [9], as highlighted in Figure 4 (m_e and m_i are the electron and ion masses, respectively). OSIRIS simulations also show that when crossing the shock, the upstream plasma is significantly heated. The observed downstream wave spectrum is thus consistent with the hypothesis of a resonant interaction between electrons and ions being driven by lower-hybrid turbulence.

While the OSIRIS simulation indicates a significant heating of the plasma, because of finite computational resources, these are performed with an electron-ion mass ratio and plasma velocity different from that of the experiment. Thus, to apply the OSIRIS results to the measured data, the simulation conditions need to be properly re-scaled to those occurring in the experiment.

The average energy of electrons accelerated by lower-hybrid waves can be estimated [9] by

$$E_e = \alpha^{2/5} \left(\frac{m_e}{m_i} \right)^{1/5} m_i u^2, \quad (1)$$

where α is an efficiency factor on the order of a few percent and u is the ion velocity (see Supplementary Information). Since OSIRIS simulations predict that lower-hybrid turbulence heats electrons to $E_e^{PIC} \sim 75$ keV, the rescaling to the laboratory conditions immediately follows from Equation 1:

$$\frac{E_e^{\text{Lab}}}{45 \text{ eV}} = \frac{E_e^{\text{PIC}}}{75 \text{ keV}} \left(\frac{m_e^{\text{Lab}}}{m_e^{\text{PIC}}} \right)^{1/5} \left(\frac{m_i^{\text{Lab}}}{m_i^{\text{PIC}}} \right)^{4/5} \left(\frac{u^{\text{Lab}}}{u^{\text{PIC}}} \right)^2, \quad (2)$$

where we have assumed the same efficiency factor both in the laboratory and

in OSIRIS simulations. For the predicted average electron heating in the laboratory is ~ 45 eV, this electron energy can then be used in Equation 1 to determine an efficiency factor of $\alpha \sim 0.1$. Our OSIRIS simulation suggests that these accelerated electrons have a nearly Gaussian spectrum. The high energy tail of this distribution is then responsible for the observed X-ray excess.

The collisional-radiative code PrismSPECT was used to calculate the X-ray emission from the predicted hot electron population of lower-hybrid electrons (see Supplementary Information). When no hot population was present, no Fluorine X-rays were obtained. As the efficiency factor α increases, the X-ray intensity of the observed Fluorine line also increases (See Figure 5). The PrismSPECT results show that an average hot electron energy of at least 30 eV is sufficient to produce the X-rays observed within the laboratory.

In the experiment, the counter-streaming Fluorine ions have a collisional mean-free-path of ~ 5 mm (See Supplementary Information), to be compared with their gyroradius ~ 2 cm. This does not affect the growth of the lower-hybrid instability [13].

Our results provide compelling evidence that lower-hybrid waves play an important role in energizing electrons and thus provide a potential mechanism for overcoming the injection problem for perpendicular shocks. We infer the presence of this electron energization by the observation of excess X-ray emission from the plasma when a magnetized sphere is present. The magnetized sphere permits the generation of lower-hybrid waves through a shock-reflected ion instability, thus allowing these waves to energize the electrons by energy transfer from the ionic motion. Whilst this electron energization process has been inferred in many astrophysical environments, it is not fully understood and so makes our experiment an important platform for the validation of the particle acceleration models frequently invoked to explain the high energy electrons

observed at strong astrophysical shocks.

Methods

Lower-hybrid waves and modified two-stream instability. Lower-hybrid waves are electrostatic ion waves that propagate quasi-perpendicularly to an external magnetic field. Lower-hybrid waves have a frequency between the ion and electron gyro frequency and can be generated through a plasma instability, namely the modified two-stream instability (MTSI) [13]. The MTSI is similar to the two-stream instability in the sense that it is formed through counter-streaming flows, however unlike the classic two-stream instability, the MTSI requires an external magnetic field oriented quasi-perpendicularly to a counter-streaming ion flow [6].

This instability excites lower-hybrid waves which have the following dispersion relation [24]:

$$\omega^2 = \omega_{LH}^2 \left(1 + \frac{\omega_{pe}^2}{k_{\perp}^2 c^2} \right)^{-1} (1 + x^2), \quad (3)$$

where ω_{LH} is the lower-hybrid frequency,

$$\omega_{LH} = \sqrt{\frac{\omega_{ci}\omega_{ce}}{1 + \left(\frac{\omega_{ce}}{\omega_{pe}}\right)^2}}, \quad (4)$$

and x is defined by

$$x^2 = \frac{m_i}{m_e} \frac{k_{\parallel}^2}{k_{\perp}^2} \left(1 + \frac{\omega_{pe}^2}{k_{\perp}^2 c^2} \right)^{-1}, \quad (5)$$

and ω_{pe} is the electron plasma frequency, k_{\parallel} and k_{\perp} are the components of the wave vector \mathbf{k} parallel and perpendicular to the magnetic field, ω_{ce} and ω_{ci} are the electron and ion cyclotron frequencies and m_i and m_e are the ion and electron masses.

These lower-hybrid waves can accelerate electrons through Cerenkov reso-

nance. Since the lower-hybrid waves travel mostly perpendicularly to the magnetic field, this wave-vector component is much larger than that of the wave-vector parallel to the magnetic field. As a consequence, the lower-hybrid waves have a high phase velocity along the field lines that resonate with fast moving electrons as well as a low phase velocity across the field lines that resonate with the slow moving ions. Consequently energy can be transferred via the lower-hybrid waves from the ions traveling perpendicular to the magnetic field to electrons traveling parallel to the field. In this manner, counter-streaming ions in an external magnetic field can accelerate electrons to large energies and so produce high energy X-rays.

Within the laboratory experiment described here, a counter-streaming ion flow is set up by reflecting ions off of the shock created at the sphere. The reflected ions and remaining incoming ions can then produce the MTSI, and so generate lower-hybrid waves. Lower-hybrid waves have been previously observed both astrophysically [10, 11, 25, 12] and in the laboratory, mostly within fusion devices [26, 27, 28].

Lower-hybrid waves in Space Plasmas.

Turning to astrophysical environments, in the passing of a comet through the Solar-wind, as described in Ref. [9], lower-hybrid waves have been invoked to explain cometary X-ray emission. In this scenario, which is equivalent to what is described in the main paper by our experiment, the interaction of the incoming Solar-wind ions with the ions reflected by the cometary bow shock excites waves within the LH frequency range. Here, the photo-ionized cometary ions are accelerated by the $\mathbf{v} \times \mathbf{B}$ electric field, where \mathbf{B} is the magnetic field of the Solar wind and \mathbf{v} is the relative velocity of cometary ions and Solar wind, these so called pick up cometary ions form a beam in the Solar wind. Electrons are heated by LH waves, producing a suprathermal electron population. This

hot electron population is estimated to have an average energy ~ 100 eV and maximum energy ~ 5 keV. These suprathermal electrons are then capable of generating bremsstrahlung and K-shell radiation from excited ions, mostly C, N and O [29].

An alternative explanation of the observed X-ray emission is offered by considering charge exchange processes [30]. In this scenario, the heavier ions in the Solar wind exchange charges with the neutral gases in the comet [20], resulting in stronger line emission. This is also supported by laboratory experiments using a beam ion trap [20].

While both lower-hybrid turbulence and charge-exchange can explain the X-ray emission in comets, only the former can account for the observed X-ray excess in our experiment. The charge exchange mechanism can be ruled out as the dominant mechanism in our experiment since it places no restriction on the presence of a magnetic field. The laboratory data shows a large excess in X-ray production only in the presence of a magnetic field perpendicular to the flow.

Comparison between the Laboratory, Space and Simulation. Whilst the properties of plasmas in laboratory and space environments are often vastly different, through appropriate scaling of the relevant parameters involved, a comparison between the two environments can be made. In Table S1 the relevant plasma parameters for this experiment, a comet interacting with the Solar-wind, and the OSIRIS simulations performed for this experiment are compared. Since the properties of greatest interest are those relating to the production of lower-hybrid waves via the MTSI, the fluorine ions only have been considered. The parameters shown in Table S1 for the interaction of a comet with the Solar-wind were chosen with the following considerations in mind. The expanding gas cloud surrounding a comet is mostly comprised of water and some carbon dioxide, meaning that the majority of the cometary ions involved are photo-

ionized oxygen ions. The temperature of the ions varies between $\sim 0.02 - 0.2$ eV, and so a value of 0.1 eV seems appropriate. The Solar-wind comprises of a slow mode with speed ~ 100 km/s. The Solar-wind contains a magnetic field of $\sim 10 - 200$ μ G and has ion temperatures of $\sim 1 - 10$ eV with electron densities of $1 - 10$ cm^{-3} . The parameters in the OSIRIS simulations are scaled to an electron density which matches the electron density in the experiment.

Table 1: **Laboratory, Space and Simulation Parameters.** Here m_p , m_e are the proton and electron mass, respectively, e is the electron charge, $\omega_{pe} = \sqrt{n_e e^2 / m_e \epsilon_0}$ is the electron plasma frequency, $c_s = \sqrt{e Z T / M + 3e T / M}$ is the sound speed and $V_A = B / \sqrt{\mu_0 (M n_i + m_e n_e)}$ is the Alfvén velocity. The length scale, L , is the minimum of the ion-beam mean free path (see Plasma Collisionality above), $V \tau_{ie}$ and the ion gyro-radius.

Quantity	Expression	Experiment	Comet-SW	OSIRIS
Ion Mass, M	–	$19 m_p$	$16 m_p$	$100 m_e$
Ion Charge, Z	–	2	1	1
Electron Density, n_e (cm^{-3})	–	$5/3 \times 10^{17}$	10	5×10^{17}
Electron and Ion Temperature, T (eV)	–	3	0.1	3
Flow Velocity, V (m/s)	–	70×10^3	100×10^3	3×10^7
Magnetic Field, B (T)	–	0.5	10^{-8}	28
Electron cyclotron frequency, ω_{ce} (rad/s)	eB/m_e	8.8×10^{10}	1.8×10^3	4.9×10^{12}
Ion cyclotron frequency, ω_{ci} (rad/s)	ZeB/M	5.0×10^6	0.060	4.9×10^{10}
Electron Larmor radius, r_{ge} (m)	$m_e V / (eB)$	8.0×10^{-7}	57	6.1×10^{-6}
Ion Larmor radius, r_{gi} (m)	$MV / (ZeB)$	0.014	1.7×10^6	6.1×10^{-4}
Sound Mach number	V/c_s	8.0	65	200
Alfvén Mach Number	V/V_A	8.0	5.8	8.0
Plasma beta	$2 \times 10^6 n_e T e \mu_0 / B^2$	0.80	4.0×10^{-3}	7.7×10^{-4}
Lower-hybrid frequency, ω_{LH} (rad/s)	Equation 4	6.7×10^8	10	4.9×10^{11}
Average electron energy (eV)	Equation 1	45	85	7.5×10^4
$r_{ge} / (c / \omega_{pe})$	–	0.061	0.037	0.81
$r_{gi} / (c / \omega_{pi})$	–	8.1	5.8	8.1
$\omega_{LH} \tau_{ie}$	–	13	1.8×10^7	7.5×10^5
$V / (L \omega_{LH})$	$L = \text{Min}(V \tau_{ie}, r_{gi})$	0.078	0.0058	0.10

Table 1 shows that whilst many of the parameters such as cyclotron frequencies and gyro radii are very different between the laboratory and astrophysical cases, scaled quantities such as the ratio of gyro-radii to skin depth, are con-

versely quite similar. The product of the lower-hybrid frequency, ω_{LH} , and the ion-beam collision time, τ_{ie} is one way of comparing the growth of the instability. Clearly in collisionless situations such as space and in OSIRIS simulations, the large time-scale between collisions makes this quantity much greater than in the mildly-collisional laboratory case. On the other hand, a comparison between the period of the lower-hybrid wave oscillations and the time it takes for an ion to interact with a lower-hybrid wave (either V/r_{gi} or τ_{ie} , depending on which quantity is smaller), is similar for all three cases.

Acknowledgements

We thank all the LULI technical staff at École Polytechnique for their support during the experiment. The research leading to these results has received funding from the European Research Council under the European Community's Seventh Framework Programme (FP7/2007-2013) / ERC grant agreements no. 256973 and 247039, AWE plc., the Engineering and Physical Sciences Research Council (grant numbers EP/M022331/1, EP/N014472/1 and EP/N002644/1) and the Science and Technology Facilities Council of the United Kingdom. F. Cruz and L. O. Silva acknowledge support from the European Research Council (InPairs ERC-2015-AdG 695088), FCT Portugal (Grant No. PD/BD/114307/2016) the Calouste Gulbenkian Foundation and PRACE for awarding access to resource MareNostrum, based in Spain at Barcelona Supercomputing Center. The PIC simulations were performed at the IST cluster (Lisbon, Portugal), and MareNostrum (Spain). This work was supported in part at the University of Chicago by the U.S. DOE NNSA ASC through the Argonne Institute for Computing in Science under FWP 57789 and the U.S. DOE Office of Science through grant No. DE- SC0016566. The software used in this work was developed in part by the DOE NNSA ASC- and DOE Office of Science ASCR-supported Flash Center for Computational Science at the University of

Chicago.

Author Contributions, G.G., B.R. A.R.B., F.F., S.L., F.M., S.S. and R.Bi. conceived this project and it was designed by G.G., S.L., and M.K. The LULI experiment was carried out by A.R., B.A., J.E.C., Y.H., P.M.K., Y.K., J.R.M., T.M., M.O., Y.S. and M.K. The paper was written by A.R., F.C., B.R. and G.G. The data was analysed by A.R. Numerical simulations were performed by F.C. and P.T. Further experimental and theoretical support was provided by R.Ba., P.G., D.Q.L., C.S., R.T. and L.O.S.

Data Availability

All raw and derived data used to support the findings of this work are available from the authors on request.

References

- [1] K. Koyama et al. *Evidence for shock acceleration of high-energy electrons in the supernova remnant SN1006*, Nature 378, 255-258, 1995
- [2] A. Masters et al. *Electron acceleration to relativistic energies at a strong quasi-parallel shock wave*, Nature Physics 9, 164-167, 2013
- [3] E. A. Helder et al. *Observational Signatures of Particle Acceleration in Supernova Remnants*, Space Science Reviews 173, 369-431, 2012
- [4] R. Blandford and D. Eichler *Particle acceleration at astrophysical shocks: A theory of cosmic ray origin*, Physics Reports 154, 1-75, 1987
- [5] R. Van Weeren et al. *Particle Acceleration on Megaparsec Scales in a Merging Galaxy Cluster*, Science 330, 347-349, 2010.
- [6] A. Marcowith et al. *The microphysics of collisionless shock waves*, Reports on Progress in Physics 79, 046901, 2016

- [7] T. Amano and M. Hoshino *Electron Injection at High Mach Number Quasi?-perpendicular Shocks: Surfing and Drift Acceleration*, The Astrophysical Journal 661, 190-202, 2007
- [8] M. Riquelme and A. Spitkovsky *Electron injection by Whistler waves in non-relativistic shocks*, The Astrophysical Journal 733, 1-15, 2011
- [9] R. Bingham et al. *Generation of X-rays from Comet C/Hyakutake 1996 B2*, Science 275, 49-51, 1997
- [10] K. G. McClements et al. *Acceleration of cosmic ray electrons by ion-excited waves at quasiperpendicular shocks*, Monthly Notices of the Royal Astronomical Society 291, 241-249, 1997
- [11] R. Bingham et al. *X-ray emission from comets, cometary knots and supernova remnants*, The Astrophysical Journal 127, 233-237, 2000
- [12] J. Vink and M. J. Laming *On the Magnetic Fields and Particle Acceleration in Cassiopeia A*, The Astrophysical Journal 584, 758-769, 2003
- [13] J. B. McBride et. al. *Theory and Simulation of Turbulent heating by the Modified Two-Stream Instability*, Physics of Fluids 15, 2367-2382, 1972
- [14] N. J. Fisch. *Theory of Current Drive in Plasmas*, Reviews of Modern Physics, Volume 59, 175-234, 1987
- [15] M. Porkolab et al. *High-Power Electron Landau-Heating Experiments in the Lower Hybrid Frequency Range in a Tokamak Plasma*, Physical Review Letters, 53, 1229-1232, 1984
- [16] R. Cesario et al. *Current drive at plasma densities required for thermonuclear reactors*, Nature Comms. 1, 1-8, 2010

- [17] J. A. Eilek and J. C. Weatherall in *Diffuse thermal and relativistic plasma in galaxy clusters*. Edited by Hans Bohringer, Luigina Feretti, Peter Schuecker. Garching, Germany: Max-Planck-Institut fur Extraterrestrische Physik, 71–76, 1999
- [18] I. H. Cairns and G. P. Zank *Turn-on of 2-3 kHz radiation beyond the heliopause*, Geophysical Research Letter 29, 47-1–47-2, 2002
- [19] Y. P. Zakharov et al. *Simulation of astrophysical plasma dynamics in the laser experiments*, AIP Conference Proceedings 369, 357-362, 2008
- [20] P. Beiersdorfer et al. *Laboratory Simulation of Charge Exchange-Produced X-ray Emission from Comets*, Science 300, 1558–1559, 2003
- [21] A. R. Bell et al. *Collisionless shock in a laser-produced ablating plasma*, Physical Review A 38, 1363–1369, 1988
- [22] R. Z. Sagdeev, *Cooperative phenomena and shock waves in collisionless plasmas*, Reviews of plasma physics 4, 23, 1966
- [23] F. Cruz et al. *Formation of collisionless shocks in magnetized plasma interaction with kinetic-scale obstacles*, Physics of Plasmas 24, 022901, 2017
- [24] Y. Omelchenko et al. *Numerical simulation of quasilinear relaxation of an ion ring and production of superthermal electrons* Soviet Journal Plasma Phys. 15 (6) June 1989
- [25] M. J. Laming *Accelerated electrons in Cassiopeia A: thermal and electromagnetic effects*, The Astrophysical Journal 563, 828–841, 2001
- [26] T. Yamamoto et al. *Experimental Observation of the rf-Driven Current by the Lower-Hybrid Wave in a Tokamak*, Physical Review letters 45, 716–719, 1980

- [27] R. L. Stenzel et al. *Electrostatic waves near the lower hybrid frequency*, Physical Review A 11, 2057–2060, 1975
- [28] R. W. Boswell et al. *Very efficient plasma generation by whistler waves near the lower hybrid frequency*, Plasma Physics and Controlled Fusion 26, 1147, 1984
- [29] M. Torney et al. *Modelling X-ray Line and Continuum Emission from Comets*, Physica Scripta, 2002, T98
- [30] T. E. Cravens et al. *Comet Hyakutake x-ray source: Charge transfer of Solar wind heavy ions*, Geophysical Research Letters 24, 105–108, 1997

Figure 1 – Illustration of a magnetized plasma-sphere interaction.

a) Interaction of a comet with the Solar-wind. The relative motion between the incoming Solar-wind ions and cometary pick-up ions, across the Solar-wind’s magnetic field, result in the formation of the modified two-stream instability (MTSI) which, in turn, can excite waves within the lower-hybrid frequency range. The lower-hybrid waves can transfer energy from the counter-streaming ions traveling perpendicular to the magnetic field into accelerating electrons parallel to the magnetic field and so produce a suprathermal electron population.

b) Schematic of the experimental setup. 1 kJ, 1.5 ns laser drive at 527 nm with a spot size of 200 μm diameter is impacted onto a 50 μm PVDF ($\text{C}_2\text{H}_2\text{F}_2$) foil target producing an expanding plasma jet from the back surface as shown in the overlaid image of the 550-800 nm optical emission of the plasma. A 12 mm diameter sphere is placed 15 mm from the target foil. The sphere is either a dipole magnetized Neodymium sphere with ≈ 7 kG surface field or a non-magnetized soda glass sphere of the same diameter. Optical diagnostics (interferometry and SOP) have ≈ 25 mm field of view, 250 ps gate time and look perpendicularly to the laser axis, similarly to the view above. An X-ray

spectrometer spatially resolves along the laser axis with an RbAP crystal and spectrally resolves within the region of 630-770 eV.

Figure 2 – Optical Data and Radiation-hydrodynamic Simulations.

a) SOP data for a non-magnetized sphere. The plasma emission in the optical band 550-800 nm along the flow axis is streaked in time for 500 ns. Vertical dashed lines indicate the position of the target and sphere; horizontal lines indicate the time at which the interferometry data and FLASH simulation snapshot were taken. The plasma reaches the sphere in 200 ns indicating a flow velocity of 70 km/s. b) Same as a) but for a magnetized sphere. c) Transverse optical interferometry data taken at 300 ns for a non-magnetized sphere. The inferred electron density colour plot is overlaid (see Supplementary Information). d) Same as c) but taken at 290 ns for a magnetized sphere. e) Snapshot of a radiation-hydrodynamic simulation with no external field after 400 ns, symmetric about the laser-axis. Pseudocolour plots of electron temperature (top) and electron density (bottom) are shown. f) Same as e) but with a constant 5 kG field perpendicular to the flow axis. Colourbars are the same for both e) and f). g) Optical emission spectra of the plasma (dark blue solid line) at 300 ns, 12 mm from the target along the flow axis for the non-magnetized sphere case. Different spectra predicted by the code PrismSPECT (dashed lines) are overlaid and give a temperature best fit of 3 ± 1 eV (see Supplementary Information).

Figure 3 – X-ray data. a) Integrated X-ray intensity of the Fluorine He- α line as a function of position along the laser axis. Data for magnetized sphere shots (blue diamonds) has an increased intensity close to the sphere when compared with data for non-magnetized sphere shots (red circles). The error bars represent that standard deviation for each data point (see Supplementary Information for further details). b) Normalized X-ray signal, showing the Fluorine He- α line for the non-magnetized (left) and magnetized (right) shots. For both

cases, a white rectangle and an additional plot have been overlaid. The white rectangle indicates the region where the spatial lineouts were taken. The overlaid plots show the average spatially-integrated spectral line shape within the white rectangle (i.e. close to the sphere). The normalization for all the X-ray data has been chosen such that the peak intensity of the spectral line shape for the magnetized sphere in case b) is set to unity.

Figure 4 – OSIRIS PIC Simulations. a) injected ion density, b) electron temperature and c) wave spectrum. The wave spectrum is calculated by performing a Fourier transform on the ion density to gain information on the parallel and perpendicular k-numbers. The black dashed lines indicate modes that have a ratio in k-number consistent with the lower-hybrid dispersion relation for ions reflected horizontally off of the shock. The black dotted lines indicate modes that have a ratio in k-number consistent with the lower-hybrid dispersion relation for ions reflected on the flanks of the bow shock. All figures are taken at the same time of 6 ion cyclotron periods.

Figure 5 – Atomic transition simulations. Results from PrismSPECT (purple line) indicate that as the hot electron population is increased in both fraction and average energy according to the efficiency factor α from Equation 1, the logged intensity of the Fluorine He- α line also increases (the average electron energy for a given value of α is shown in the top horizontal axis for reference). When no hot electron population is present, no Fluorine He- α line is generated. There is minimal contribution from bremsstrahlung. The average hot electron energy ($E_e \sim 45$ eV) and efficiency factor ($\alpha \sim 0.1$) for laboratory conditions is indicated with the black dashed line.

Supplementary Information
Optical Diagnostics.

The SOP diagnostic was setup such that plasma emission in the 550-800 nm optical band along the laser axis was streaked in time for 500 ns. The SOP data can be used to infer the velocity of the plasma flow from the foil. The emission from the laser-drive can be seen clearly at 0 ns in Figures 2a,b. At 210 ± 10 ns, there is strong plasma emission at the sphere, indicating that the plasma has traveled the 15 mm from the foil-target to the sphere, thus indicating a flow velocity of 70 ± 3 km/s. The SOP data shown in Figures 2a,b indicates the presence of transients between 200-300 ns. These transients are present in both the magnetized and non-magnetized cases and so are caused by the interaction of the plasma with the sphere, not by the magnetic field.

The Mach-Zender interferometry diagnostic was implemented using a 2ω Quantaray laser. The interferometry diagnostic had a ≈ 25 mm field-of-view, 250 ps gate time and looked perpendicularly to the laser axis (similarly to the view shown in Figure 1b). A reference image with no plasma present was taken before each laser-shot. The difference between the pre-shot image and on-shot image can then be used to infer the electron density. The electron density colour maps were generated using the Interferometric Data Evaluation Algorithm (IDEA) software. Lineouts of the electron density along the laser-axis for these two cases are shown in Figure S1 (see also Figures 2c,d). The electron density rises sharply close to the sphere in the magnetized case, but streams smoothly around the sphere in the non-magnetized case and so the electron density remains roughly constant. We notice, however, that shot-to-shot variations and noise in the interferometry data are $3-7 \times 10^{17} \text{ cm}^{-3}$, and so taking a bulk electron density $5 \times 10^{17} \text{ cm}^{-3}$ in the upstream flow is appropriate.

The optical spectroscopy diagnostic spectrally resolved the optical emission of the plasma on the laser axis, 12 mm from the target foil. The absolute spectral response of the diagnostic was made using a white light calibration, enabling the true spectrum to be recovered from the raw data. The optical spectrum was then fitted using the PrismSPECT software.

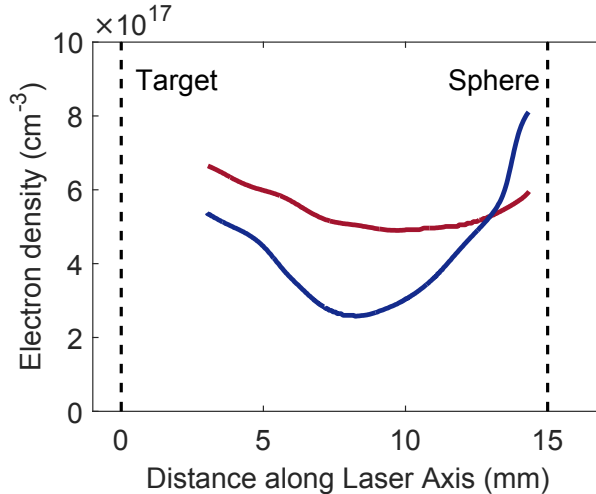


Figure S1: **Electron density profiles.** Electron density lineouts taken along the the laser-axis for the magnetized (blue) at 290 ns and non-magnetized (red) shot at 300 ns.

PrismSPECT Simulations: Optical Spectroscopy. The collisional-radiative code PrismSPECT [31] was used to fit the optical spectroscopy data. An electron density of $5 \times 10^{17} \text{ cm}^{-3}$ was used although the fits are broadly insensitive to electron density in the range 10^{17} - 10^{18} cm^{-3} . From Figure 2g, it can be seen that temperatures of 2-4 eV fit the data whilst temperatures of 1 eV and 5 eV do not match the data. A bulk electron temperature of 3 ± 1 eV best fits the data.

FLASH Radiation-Hydrodynamic Simulations 2-dimensional, radiation-magnetohydrodynamic simulations were performed using the publicly available code FLASH. FLASH is a parallel, multi-physics, adaptive-mesh-refinement (AMR), finite-volume Eulerian code. The simulations performed here include many of the high-energy density capabilities of the code [32], such as three-temperature MHD solvers, non-ideal MHD effects such as magnetic resistivity, heat exchange between ions and electrons, implicit thermal conduction and radiation transport in the multi-group diffusion approximation, and laser energy deposition via inverse Bremsstrahlung.

The FLASH simulations [32] were set up to fully reproduce the laser-plasma interaction and the resulting flow expansion and collision with the obstacle. We have performed simulations with and without a constant ambient

field of 5 kG strength orientated perpendicularly to the laser axis, which emulates the dipole field of the experiment within the region adjacent to the sphere. simulations were set up such that the computational domain ($2 \text{ cm} \times 4 \text{ cm}$) was symmetric about the laser-axis and, utilizing FLASHs AMR, we were able to resolve spatial scales down to $8 \mu\text{m}$. Spatial reconstruction was carried out using a 3rd-order piecewise parabolic method (PPM) [33] and a minmod limiter, while temporal integration was done with the second-order unsplit USM algorithm [34]. The upwind fluxes were computed using the Harten-Lax-van Leer Contact (HLLC) [35] Riemann solver. We carried out the simulations using the SCARF-MagnaCarta cluster at the Rutherford Appleton Laboratory and the Asterix cluster of the Flash Center for Computational Science at the University of Chicago.

The simulation predictions closely resemble what was observed in the experiment. The plasma outflow from the foil target travels at 70 km/s , reaching the sphere at $\sim 200 \text{ ns}$, as seen in the experimental data. In both the field and non-field cases, a shock forms at the sphere surface. Similarly to the experiment, the non-field case results in a much thinner bow-like shock than the field case. As shown in Figure 2 of the paper, the simulation predicts bulk electron densities $\sim 5 \times 10^{17} \text{ cm}^{-3}$, rising to over 10^{18} cm^{-3} at the shock front, in agreement with the laboratory data. Additionally, at the time and spatial position that the optical spectroscopy data was taken, FLASH predicts an electron temperature of 3 eV , matching the experiment. The quantitative agreement between simulation and experiment gives us confidence in the accuracy of the electron temperature predictions from the FLASH code. The electron temperature is $\sim 200 \text{ eV}$ at the beginning of the laser drive, but then it adiabatically cools to a bulk electron temperature $\sim 3 \text{ eV}$ for times $t > 50 \text{ ns}$.

Electric Field Calculation The FLASH simulations can be used to gain insight into the nature of the shock formation. Although the FLASH simulations did not include the dipole magnetic field of the obstacle, the constant field used in the simulations can give an indication of the strength of the electric field produced at the shock.

The electric field influencing the plasma near the sphere can be estimated using [22] $E_{\parallel} \sim \frac{1}{2\mu_0 n_i e} \frac{dB_{\perp}^2}{dx}$, where E_{\parallel} is the electric field parallel to the flow axis, n_i is the ion density and B_{\perp} is the magnetic field perpendicular to the flow axis and the derivative is taken along the flow axis direction.

X-ray Spectrometer Setup

The X-ray spectrometer consisted of a $25 \times 50 \text{ mm}^2$ RbAP crystal, with 100 mm radius of curvature, operating at a Bragg angle of 43.5° and is cylindrically bent along the long axis of the crystal. In this Von-Hamos geometry, the X-rays from the plasma are focused onto a $60 \times 100 \text{ mm}^2$ image plate detector as shown in Figure S1. This setup allows for both spectral resolution ($620\text{--}770 \text{ eV}$ full range) and spatial discrimination with 1:1 magnification [36]. By geometrical considerations [36], it is possible to show that a 1 mm source size is blurred on the image plane by $20 \mu\text{m}$. Both the crystal and image plate were housed in a light-tight enclosure containing a small window through which the X-rays from the sample could reach the crystal (see Figure S1). The window was filtered with $5 \mu\text{m}$ of Aluminium.

The raw signal on the image plate was analysed in the following manner. First, the background noise across each data set was removed. The background signal varies linearly along both the horizontal and vertical axes of the image plate. This background can be readily subtracted from the data signal. To calibrate the energy scale along the image plate, both PVDF and CH foils, placed at the focal position of the spectrometer, were used as shown in Figure S1. The PVDF foil produces a fluorine line at 731 eV (similarly to the main experiment). The CH foil (as expected) does not produce a line at 731 eV . Traces of Oxygen present in the vacuum chamber (rather than in the material content of the target) produce lines at 653 eV , 664 eV and 698 eV that can be seen on the image plate.

The background corrected data showed a clear line at 731 eV for all shots, the Fluorine He- α line. For every shot, the signal from the Fluorine He- α line at a given distance from the sphere has been frequency-integrated and averaged over a 0.3 mm interval. To collate the results, data from shots with the same type of sphere were averaged together. To aid comparison, different data sets are rescaled such that the peak of the spectrally resolved emission in the region close to the sphere (as shown in Figure 3) for the magnetized case is set to unity.

The standard deviation of the signal within the 0.3 mm spatial band determines the primary error for each data point as shown in Figure 3. Additionally, since the final data points are an average of several shots, the overall error is the sum in quadrature of the error for individual shots.

OSIRIS PIC Simulations. In these OSIRIS [37] PIC simulations, a hydrogen plasma is injected continuously from the left hand boundary with temperature $T_e = T_i \simeq 3 \text{ eV}$ and velocity v_0 . Due to the high computational costs, OSIRIS simulations were performed with a flow velocity $\frac{v_0}{c} = 0.1$ and an electron-ion mass ratio of $\frac{m_i}{m_e} = 100$, where m_i is the average ion mass and m_e is the electron mass. As discussed in the main text, the simulation results need to be scaled back to laboratory conditions. We have also assumed there is an externally applied magnetic field $\mathbf{B} = \mathbf{B}_0 + \mathbf{B}_d$, where \mathbf{B}_d is the sphere dipolar field (modeled in the simulation plane) and \mathbf{B}_0 is an upstream magnetic field with a magnitude chosen such that the ion Larmor radius is $\rho_i \simeq 8c/\omega_{pi}$ (where ω_{pi} is the ion plasma frequency), similarly to experimental conditions at the shock position. The simulation domain

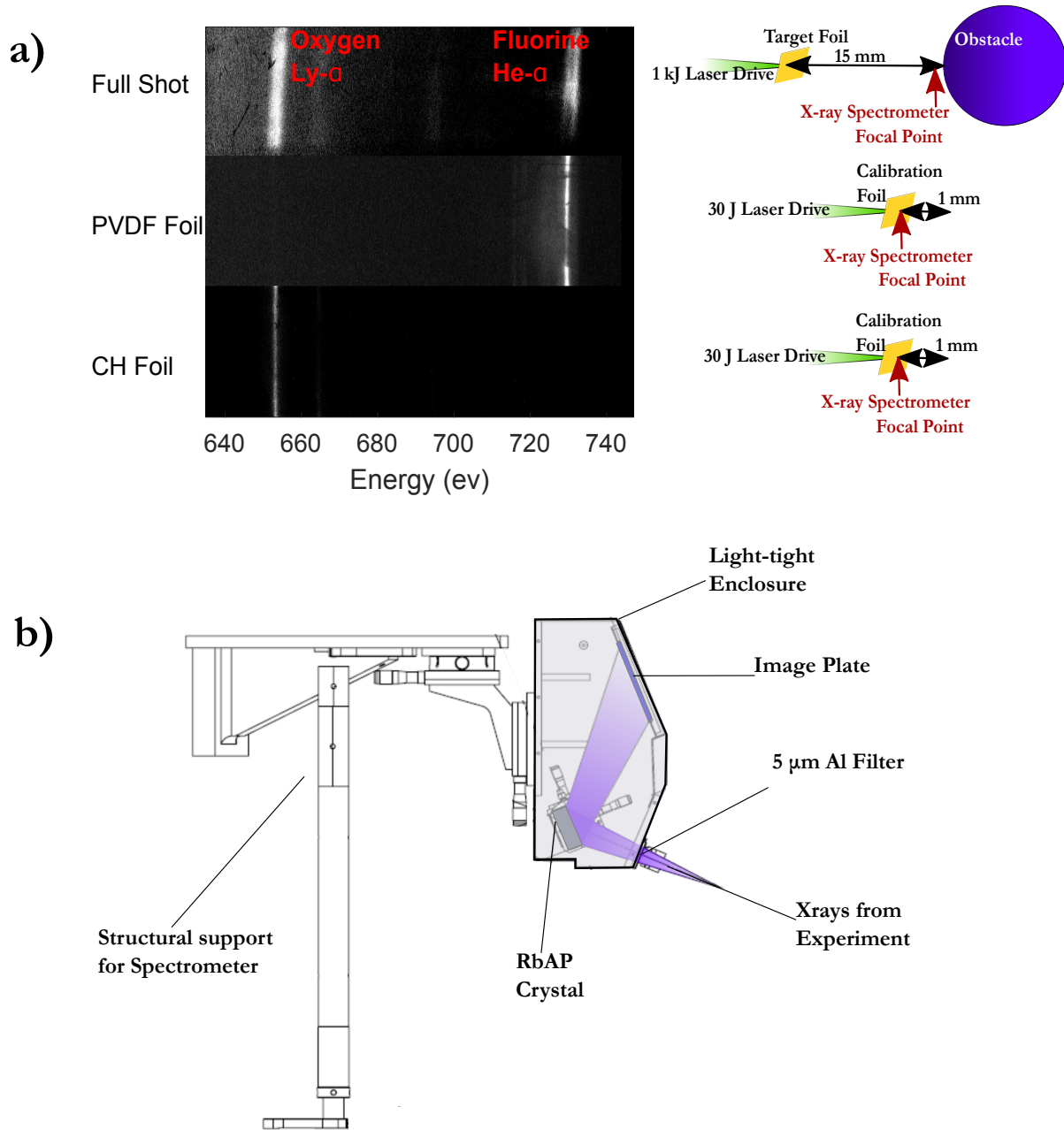


Figure S2: **X-ray Spectrometer setup and Calibration.** a) Spectra from PVDF and CH foil shots and a full shot. The foil shots can be used for calibrating the energy of the X-rays. Experimental setup for the PVDF and CH calibration foil shots. The foil is positioned at the focal point of the X-ray spectrometer, 1 mm from the sphere position. For these shots, no sphere is present. b) Schematic of X-ray spectrometer, including how the crystal is housed.

has dimensions $L_x \times L_y = 960 \times 1600c/\omega_{pe}$ and the grid resolution is 10 cells per c/ω_{pe} in both directions, with 25 simulation particles per cell per species. Periodic boundary conditions are used in the y direction, and open boundary conditions are used for the right hand boundary. Figures 4 a) and b) show only a fraction of the simulation domain.

The plasma ions are reflected at the shock front and travel upstream to a distance of the order of the ion Larmor radius. The electron temperature was extracted from the OSIRIS simulations by mapping the electron distribution function in space and computing its second central moment. The downstream temperature was found to be 10–100 keV and is maximum at the bow shock flanks.

The convergence of OSIRIS simulations with scaled up/down plasma velocities/ion-electron mass ratios has been confirmed by comparing the results of previous simulations similar to the one presented here with plasma fluid velocities down to $0.02c$ and ion-electron mass ratios up to $m_i/m_e = 900$ (see [23]). These parameters, in particular the ion-electron mass ratio, control the separation between ion and electron temporal and spatial scales. Scaling them appropriately allows a significant reduction of the computational effort to perform the numerical experiments, yet we are still able to gain important physical insight into the dynamics of these complex systems.

A more accurate description of the experiment could be obtained by using, for example, a multi-species plasma. In particular, the interaction between the different species with the field at different times is expected to lead to a transient. However, the transient always happens when the plasma cavity is formed and before the turbulent region is excited (which happens on ~ 1 ion gyroperiods, in the collisionless limit). Whether this transient time can be extended with the introduction of a multi species plasma is an interesting question, but one very difficult to answer with full PIC simulations. This would require separating clearly the time scales of the different ion species, which is computationally extremely demanding.

Despite the OSIRIS simulations being collisionless and the laboratory plasma being mildly thermally collisional, the OSIRIS results can still be applied to the laboratory plasma. The electron-electron collisions in the laboratory plasma preserve the electron isotropy and so the temperature anisotropy as seen in the OSIRIS simulations will be less pronounced in the laboratory plasma. The electron-electron collisions do not inhibit the development of the modified two-stream instability (see Plasma Collisionality below) and so the average hot electron energy in the OSIRIS simulations (75 keV) can still be scaled to laboratory conditions to give a reasonable estimate of the average hot electron energy in the laboratory (45 eV), see Equation 2.

Average electron energy Calculation. First the average energy gain of the electrons accelerated by lower-hybrid turbulence [9] is estimated. Assuming that the energy is transferred from the ions to the electrons with an efficiency factor α , energy flow balance requires that

$$\alpha n_i m_i u^3 = n_e E_e \sqrt{\frac{E_e}{m_e}}, \quad (\text{S1})$$

where n_i and n_e are the ion and electron densities of the resonant particles, u is the ion velocity, and E_e is the resonant electron energy. The resonant electron density can be obtained by balancing the growth rate of the ion instability against Landau damping due to electrons moving parallel to the magnetic field, hence

$$n_e = E_e \frac{n_i}{m_i u^2}. \quad (\text{S2})$$

Equations S1 and S2 can then be combined to give Equation 1.

PrismSPECT Simulations: X-ray Spectroscopy. PrismSPECT was used to calculate the X-ray emission from the predicted energetic electron population of lower-hybrid accelerated electrons. The PrismSPECT calculation uses a bulk plasma electron density of $5 \times 10^{17} \text{ cm}^{-3}$ and electron temperature of 3 eV, for a range of efficiency factors α from 0–0.5. For a given α , the energetic electron population had a Maxwellian distribution with average energy given by Equation 1 and density given by Equation S2.

Plasma collisionality.

Since the thermal background is relatively cold compared with the velocity of the reflected ions, the reflected ions will be dragged by the electrons in the thermal plasma and so the ion-electron collision mean-free-path (note not the thermal collision mean-free-path) is the most important quantity in determining whether or not the modified two-stream instability will be damped by collisions. Using PrismSPECT, a downstream plasma electron density of 10^{17} cm^{-3} and 3 eV electron temperature, the ionisation of the Carbon, Hydrogen and Fluorine ions is 3, 1 and 2 respectively. The ion-electron collision distance for the electrons to slow down the beam of reflected ions can be calculated using standard expressions. We note that for our case, the thermal energy of the electrons is large compared to the reflected ion beam energy.

For the three different ions, this calculation gives a distance for the ions to be slowed down by electron collisions as 1, 1.5 and 5 mm for the Hydrogen, Carbon and Fluorine ions respectively. This means that for a 3 eV background plasma, the Hydrogen and Carbon reflected ions will be slowed down within ~ 1 mm, whereas the Fluorine ions are effectively collisionless on the scales of interest for electron heating. Electron-electron collisions on the other-hand are the dominant mechanism for electron scattering. Although the electrons are only weakly magnetized ($\omega_g \tau_e \lesssim 1$), they can be accurately treated as an isotropic fluid, and as such, can be shown to satisfy the usual fluid limit of the lower-hybrid instability [13]. The ~ 30 eV electrons, inferred from PrismSPECT simulations, on the other hand will be magnetised in the strong pre-shock fields. However, their gyro-radii are still not sufficient to permit collisionless transport across the shock [38].

Comparison between the Laboratory, Space and Simulation

Table S1: **Laboratory, Space and Simulation Parameters.** Here m_p , m_e are the proton and electron mass, respectively, e is the electron charge, $\omega_{pe} = \sqrt{n_e e^2 / m_e \epsilon_0}$ is the electron plasma frequency, $c_s = \sqrt{e Z T / M + 3 e T / M}$ is the sound speed and $V_A = B / \sqrt{\mu_0 (M n_i + m_e n_e)}$ is the Alfvén velocity. The length scale, L , is the minimum of the ion-beam mean free path (see Plasma Collisionality above), $V \tau_{ie}$ and the ion gyro-radius.

Quantity	Expression	Experiment	Comet-SW	OSIRIS
Ion Mass, M	–	$19 m_p$	$16 m_p$	$100 m_e$
Ion Charge, Z	–	2	1	1
Electron Density, n_e (cm^{-3})	–	$5/3 \times 10^{17}$	10	5×10^{17}
Electron and Ion Temperature, T (eV)	–	3	0.1	3
Flow Velocity, V (m/s)	–	70×10^3	100×10^3	3×10^7
Magnetic Field, B (T)	–	0.5	10^{-8}	28
Electron cyclotron frequency, ω_{ce} (rad/s)	eB/m_e	8.8×10^{10}	1.8×10^3	4.9×10^{12}
Ion cyclotron frequency, ω_{ci} (rad/s)	ZeB/M	5.0×10^6	0.060	4.9×10^{10}
Electron Larmor radius, r_{ge} (m)	$m_e V / (eB)$	8.0×10^{-7}	57	6.1×10^{-6}
Ion Larmor radius, r_{gi} (m)	$MV / (ZeB)$	0.014	1.7×10^6	6.1×10^{-4}
Sound Mach number	V/c_s	8.0	65	200
Alfvén Mach Number	V/V_A	8.0	5.8	8.0
Plasma beta	$2 \times 10^6 n_e T e \mu_0 / B^2$	0.80	4.0×10^{-3}	7.7×10^{-4}
Lower-hybrid frequency, ω_{LH} (rad/s)	Equation 4	6.7×10^8	10	4.9×10^{11}
Average electron energy (eV)	Equation 1	45	85	7.5×10^4
$r_{ge} / (c/\omega_{pe})$	–	0.061	0.037	0.81
$r_{gi} / (c/\omega_{pi})$	–	8.1	5.8	8.1
$\omega_{LH} \tau_{ie}$	–	13	1.8×10^7	7.5×10^5
$V / (L \omega_{LH})$	$L = \text{Min}(V \tau_{ie}, r_{gi})$	0.078	0.0058	0.10

References

- [1] K. Koyama et al. *Evidence for shock acceleration of high-energy electrons in the supernova remnant SN1006*, Nature 378, 255-258, 1995
- [2] A. Masters et al. *Electron acceleration to relativistic energies at a strong quasi-parallel shock wave*, Nature Physics 9, 164-167, 2013
- [3] E. A. Helder et al. *Observational Signatures of Particle Acceleration in Supernova Remnants*, Space Science Reviews 173, 369–431, 2012
- [4] R. Blandford and D. Eichler *Particle acceleration at astrophysical shocks: A theory of cosmic ray origin*, Physics Reports 154, 1–75, 1987
- [5] R. Van Weeren et al. *Particle Acceleration on Megaparsec Scales in a Merging Galaxy Cluster*, Science 330, 347-349, 2010.
- [6] A. Marcowith et al. *The microphysics of collisionless shock waves*, Reports on Progress in Physics 79, 046901, 2016
- [7] T. Amano and M. Hoshino *Electron Injection at High Mach Number Quasi-perpendicular Shocks: Surfing and Drift Acceleration*, The Astrophysical Journal 661, 190-202, 2007
- [8] M. Riquelme and A. Spitkovsky *Electron injection by Whistler waves in non-relativistic shocks*, The Astrophysical Journal 733, 1–15, 2011
- [9] R. Bingham et al. *Generation of X-rays from Comet C/Hyakutake 1996 B2*, Science 275, 49–51, 1997
- [10] K. G. McClements et al. *Acceleration of cosmic ray electrons by ion-excited waves at quasiperpendicular shocks*, Monthly Notices of the Royal Astronomical Society 291, 241–249, 1997
- [11] R. Bingham et al. *X-ray emission from comets, cometary knots and supernova remnants*, The Astrophysical Journal 127, 233-237, 2000

- [12] J. Vink and M. J. Laming *On the Magnetic Fields and Particle Acceleration in Cassiopeia A*, The Astrophysical Journal 584, 758-769, 2003
- [13] J. B. McBride et. al. *Theory and Simulation of Turbulent heating by the Modified Two-Stream Instability*, Physics of Fluids 15, 2367–2382, 1972
- [14] N. J. Fisch. *Theory of Current Drive in Plasmas*, Reviews of Modern Physics, Volume 59, 175–234, 1987
- [15] M. Porkolab et al. *High-Power Electron Landau-Heating Experiments in the Lower Hybrid Frequency Range in a Tokamak Plasma*, Physical Review Letters, 53, 1229–1232, 1984
- [16] R. Cesario et al. *Current drive at plasma densities required for thermonuclear reactors*, Nature Comms. 1, 1–8, 2010
- [17] J. A. Eilek and J. C. Weatherall in *Diffuse thermal and relativistic plasma in galaxy clusters*. Edited by Hans Bohringer, Luigina Feretti, Peter Schuecker. Garching, Germany: Max-Planck-Institut fur Extraterrestrische Physik, 71–76, 1999
- [18] I. H. Cairns and G. P. Zank *Turn-on of 2-3 kHz radiation beyond the heliopause*, Geophysical Research Letter 29, 47-1–47-2, 2002
- [19] Y. P. Zakharov et al. *Simulation of astrophysical plasma dynamics in the laser experiments*, AIP Conference Proceedings 369, 357-362, 2008
- [20] P. Beiersdorfer et al. *Laboratory Simulation of Charge Exchange-Produced X-ray Emission from Comets*, Science 300, 1558–1559, 2003
- [21] A. R. Bell et al. *Collisionless shock in a laser-produced ablating plasma*, Physical Review A 38, 1363–1369, 1988
- [22] R. Z. Sagdeev, *Cooperative phenomena and shock waves in collisionless plasmas*, Reviews of plasma physics 4, 23, 1966
- [23] F. Cruz et al. *Formation of collisionless shocks in magnetized plasma interaction with kinetic-scale obstacles*, Physics of Plasmas 24, 022901, 2017
- [24] Y. Omelchenko et al. *Numerical simulation of quasilinear relaxation of an ion ring and production of superthermal electrons* Soviet Journal Plasma Phys. 15 (6) June 1989
- [25] M. J. Laming *Accelerated electrons in Cassiopeia A: thermal and electromagnetic effects*, The Astrophysical Journal 563, 828–841, 2001
- [26] T. Yamamoto et al. *Experimental Observation of the rf-Driven Current by the Lower-Hybrid Wave in a Tokamak*, Physical Review letters 45, 716–719, 1980
- [27] R. L. Stenzel et al. *Electrostatic waves near the lower hybrid frequency*, Physical Review A 11, 2057–2060, 1975
- [28] R. W. Boswell et al. *Very efficient plasma generation by whistler waves near the lower hybrid frequency*, Plasma Physics and Controlled Fusion 26, 1147, 1984
- [29] M. Torney et al. *Modelling X-ray Line and Continuum Emission from Comets*, Physica Scripta, 2002, T98
- [30] T. E. Cravens et al. *Comet Hyakutake x-ray source: Charge transfer of Solar wind heavy ions*, Geophysical Research Letters 24, 105–108, 1997
- [31] J. J. MacFarlane et al. *SPECT3D - A multi-dimensional collisional-radiative code for generating diagnostic signatures based on hydrodynamics and PIC simulation output*, High Energy Density Physics 3, 181-190, 2007
- [32] P. Tzeferacos et al. *FLASH MHD simulations of experiments that study shock-generated magnetic fields*, High Energy Density Physics 17, 24-31, 2015
- [33] P. Colella et al. *The piecewise parabolic method (PPM) for gas-dynamical simulations*, Journal of Computational Physics 54, 174–201, 1984

- [34] D. Lee *An implicit ghost-cell immersed boundary method for simulations of moving body problems with control of spurious force oscillations*, Journal of Computational Physics 233, 295–314, 2013
- [35] S. Li *An HLLC Riemann solver for magneto-hydrodynamics*, Journal of Computational Physics 203, 344–357, 2005
- [36] A. P. Shevelko *X-Ray Spectroscopy of laser-produced plasmas using a von Hamos spectrograph*, Proc. SPIE 3406, 91–109, 1998
- [37] R. A. Fonseca et al. *OSIRIS: A Three-Dimensional, Fully Relativistic Particle in Cell Code for Modeling Plasma Based Accelerators*, Lecture Notes in Computer Science 2331, 342-351, 2002
- [38] G. Gregori et al. *The generation and amplification of intergalactic magnetic fields in analogue laboratory experiments with high power lasers*, Physics Reports 601, 1–34, 2015